

Climate change projections over China using regional climate models forced by two CMIP5 global models. Part II: projections of future climate

Pinhong Hui,^a Jianping Tang,^{b*} Shuyu Wang,^{b*} Xiaorui Niu,^b Peishu Zong^c and Xinning Dong^d

^a Jiangsu Climate Center, Jiangsu Provincial Meteorological Bureau, Nanjing, China

^b CMA-NJU Joint Laboratory for Climate Prediction Studies, Institute for Climate and Global Change Research, School of Atmospheric Sciences, Nanjing University, Nanjing, China

^c Jiangsu Meteorological Observatory, Jiangsu Provincial Meteorological Bureau, Nanjing, China

^d Chongqing Climate Center, Chongqing Meteorological Bureau, Chongqing, China

ABSTRACT: The changes in mean and extreme climate in China during 2020–2060 are detected with both Weather Research and Forecasting and RegCM4, by downscaling the simulations from EC-EARTH and IPSL-CM5A under both the RCP4.5 and RCP8.5 scenarios. The climate changes under the two scenarios exhibit similar patterns, with stronger intensity under the RCP8.5 scenario. For the mean precipitation, increases are projected in most regions, with the largest relative increase in the Tarim Basin. Slight drought mainly occurs in the south-eastern part of China. The frequency of drizzle rain is expected to decrease in all the sub-regions, but the moderate to heavy rainfall as well as the storm would occur more frequently, especially on the Tibetan Plateau. The whole country would experience much warmer climate in the future, with the strongest warming over the Tibetan Plateau. By detecting the changes in climate extremes, it is indicated that less dry extremes would occur in the wet areas of China, while more dry events in the arid and semiarid regions. The wet extreme indices would increase in most regions, especially in the wet areas. The surface air temperature tends to become extremely warmer in the future over the whole country, with the strongest change over the Tibetan Plateau. The changes in mean and extreme climate depend strongly on the driving global climate models, with wetter and warmer climate in the downscalings over IPSL-CM5A, and the model physics of the regional climate models also exert great impact on the projections. Finally, the possible mechanisms for the changes of extreme precipitation are discussed. The enhanced summer monsoon in the future transports more moisture to China, which could lead to more summer precipitation. As a result, the wet extremes tend to increase.

KEY WORDS climate change; dynamical downscaling; different RCMs; CMIP5 global models; RCP scenarios

Received 17 August 2017; Revised 7 November 2017; Accepted 15 December 2017

1. Introduction

According to the Intergovernmental Panel on Climate Change (IPCC)'s Fifth Assessment Report (AR5), the global average surface air temperature will increase by 0.3–4.8 °C in the 21st century (IPCC, 2013). Many studies based on observations and climate models have indicated that the global warming is accelerated because of the anthropogenic factors (Giorgi and Mearns, 1999; Easterling *et al.*, 2000; Suh and Lee, 2004; Bao, 2012; IPCC, 2013). Also the extreme climate events have also increased, which can be attributed to the global warming (Easterling *et al.*, 2000; Alexander *et al.*, 2006; Kim *et al.*, 2009; Shiogama *et al.*, 2010; IPCC, 2013; Jeong *et al.*, 2014). China is located in the East Asian Monsoon

region and features with frequent occurrence of abnormal weather and climate events, and most part of the country is vulnerable to climate change (Editorial Committee of National Assessment Report of Climate Change, 2011). To maintain the sustainable development, it is essential for the climate community to provide reliable projections for both the mean and extreme climates in the future. Such information would be valuable for adaption planning and impact assessment studies.

Great efforts and important progresses have been made to produce reliable regional climate in the future during the past decades. Among them is the development and application of dynamical downscaling, which uses regional climate models (RCMs) to provide fine-scale climate information based on the outputs from global climate models (GCMs) with coarse resolution (Giorgi *et al.*, 2001; Gao *et al.*, 2012b). RCMs have been proven to be capable of improving the representations of mean climatology and extreme climate over GCMs, and widely used in regional climate change projection over East Asia

* Correspondence to: J. Tang or S. Wang, CMA-NJU Joint Laboratory for Climate Prediction Studies, Institute for Climate and Global Change Research, School of Atmospheric Sciences, Nanjing University, Xianlin Campus, 163 Xianlin Road, Nanjing 210023, China. E-mail: jptang@nju.edu.cn; wsy@nju.edu.cn

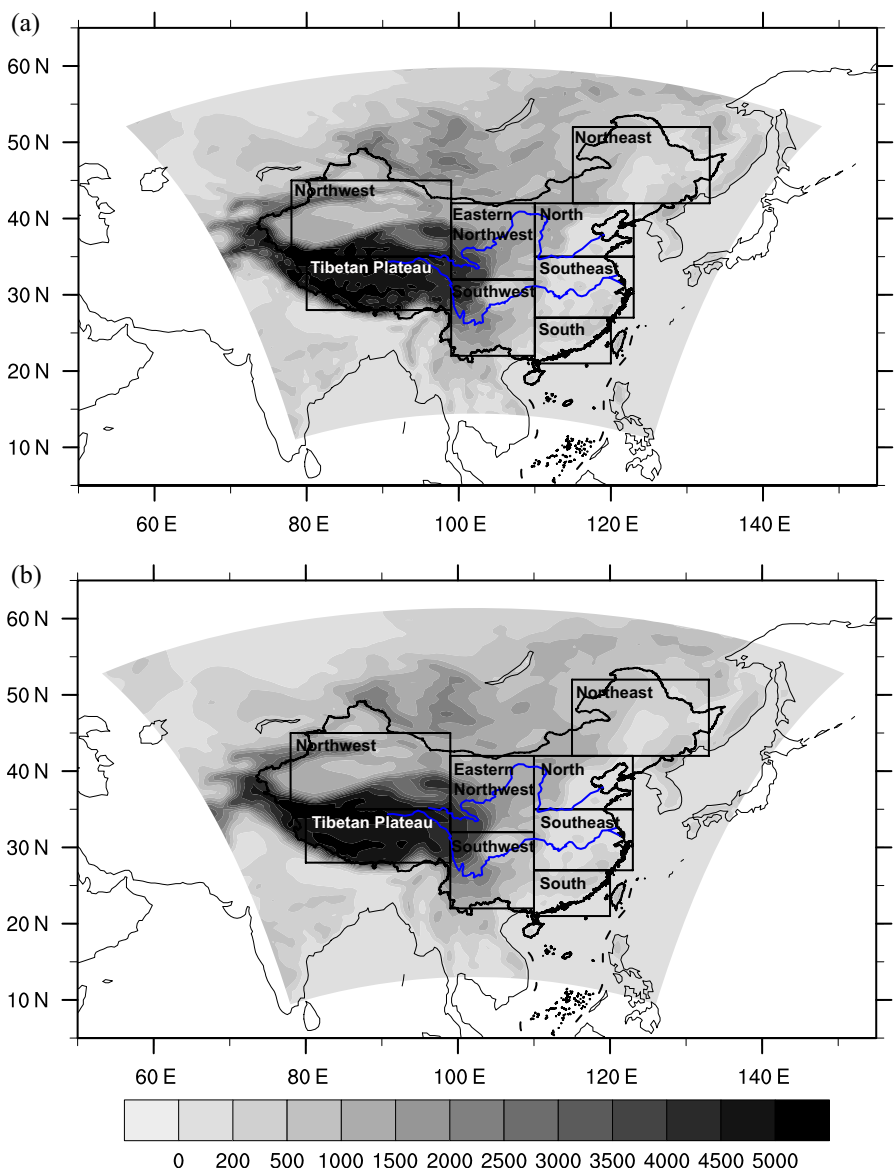


Figure 1. Simulation domain and the topography within it (grey shading, unit: m) for WRF (a) and RegCM4 (b). The eight sub-regions are marked with black rectangles.

including China (e.g. Zou and Zhou, 2013; Bao *et al.*, 2015; Andrys *et al.*, 2016; Qin and Xie, 2016; Smiatek *et al.*, 2016; Tang *et al.*, 2016; Yang *et al.*, 2016). For example, Bao *et al.* (2015) assessed the present-day and future precipitation changes over China using the Weather Research and Forecasting (WRF) model driven with GFDL-ESM2G under the RCP4.5 scenario, indicating increase of annual and extreme precipitation in most parts of China. With RegCM4 (Regional Climate Model system version 4) forced by the GCM GFDL_ESM2M under the RCP4.5 scenario, Qin and Xie (2016) projected more wet extremes as well, especially in southeast China in the middle 21st century. They further demonstrated that the precipitation extreme indices are sensitive to the annual and seasonal mean precipitation, total water vapour, and upward vertical wind.

Although the RCMs show their reliabilities in the regional climate projections, uncertainties in the projected

regional climate changes arise from various sources, including the driving GCMs, emission scenarios and natural climate internal variabilities (Déqué *et al.*, 2007; Deser *et al.*, 2012). Systematic studies have been performed to quantify and reduce the uncertainties in the regional climate projections (e.g. Déqué *et al.*, 2007; Marengo *et al.*, 2010; Gao *et al.*, 2012a; Wang *et al.*, 2014; Niu *et al.*, 2015; Wu and Huang, 2016). In China, significant contributions of driving GCMs to the uncertainties in precipitation change were detected by Gao *et al.* (2012a), using one RCM to downscale multi-GCMs for the precipitation change projections. Niu *et al.* (2015) constructed future precipitation in China using five RCMs driven by the one GCM, and found that similar changes in summer precipitation were projected by all RCMs over western China, but model behaviours were quite different over eastern China of the Eastern Asian Summer Monsoon region.

Table 1. Experiment design for the downscaling simulations.

	WRF	RegCM4
Governing equations	Non-hydrostatic	Hydrostatic
Initial and boundary conditions	EC-EARTH, IPSL-CM5A	EC-EARTH, IPSL-CM5A
Cumulus convection	Kain–Fritsch	MIT-Emanuel
Microphysics	WSM5	None
Radiation	CAM	CCM3
Land surface	NOAH	CLM
Planet boundary layer	YSU	Holtslag
Domain centre	36.5°N, 102°E	36.5°N, 102°E
Grids and resolution	117 × 103, 50 km	124 × 112, 50 km
Simulation period	2019–2060	2019–2060

Previous studies have investigated the uncertainties in regional climate projections of precipitation arising from various sources, such as the scenarios, the driving GCMs and the model physics of RCMs. In order to increase the reliability of the climate change simulation, more efforts should be made to understand the relative importance of the contributions from different sources. In Part I of this research (Hui *et al.*, 2018), the Coupled Model Intercomparison Project phase 5 (CMIP5) models of EC-EARTH and IPSL-CM5A (Institute Pierre Simon Laplace-Climate Model version 5A) were downscaled with RegCM4 and WRF over China for the present period of 1980–2000. In general, improvements are brought out by the downscalings in many aspects, especially over IPSL-CM5A. In addition, the added value of the RCMs depends on the season and the geophysical location over the country. Following the work in Part I, this study performs dynamical downscaling projections for the climate change in China over the period of 2020–2060, and the projections are carried out under both the RCP4.5 and RCP8.5 scenarios. The rest of the paper is organized as follows: observational data sets and experimental design is introduced in Section 2. Section 3 presents the analysis results and Section 4 gives a summary of the main conclusions in the paper.

2. Methodology

2.1. Description of the GCMs

The initial and lateral boundary conditions of two RCMs are derived from the projections of the global models of EC-EARTH and IPSL-CM5A in CMIP5 (Taylor *et al.*, 2012). EC-EARTH is based on European Centre for Medium-Range Weather Forecasts (ECMWF's) seasonal forecasting system 3 (Hazeleger *et al.*, 2010), and coupled to the NEMO version 2, an ocean model developed by the Institute Pierre Simon Laplace (IPSL) in France (Madec, 2008). Its spectral horizontal resolution is T159, which is roughly $1.125^\circ \times 1.125^\circ$, with 62 vertical levels. Clouds are described by prognostic equations for cloud

water content and cloud fraction, and the convective and stratiform clouds are distinguished (Tiedtke, 1993).

IPSL-CM5A is a state-of-the-art coupled GCM developed by the IPSL (Dufresne *et al.*, 2013). It is a coupled climate model consist of four components: the LMDZ5A atmospheric model (Hourdin *et al.*, 2013); the NEMOv3.2 ocean model (Madec, 2008); the LIM2 sea-ice model (Louvain-la-Neuve Sea Ice Model) (Fichefet and Morales-Maqueda, 1997); and the Organizing Carbon and Hydrology in Dynamic Ecosystems land surface model (Krinner *et al.*, 2005). IPSL-CM5A couples the ocean, atmosphere, land, and sea ice using the OASIS3 coupler (Valcke, 2006). It generally performs well at a global scale and in East Asia (Chen *et al.*, 2011).

2.2. Experimental design

There are two RCMs used in this study. The WRF model with Advanced Research WRF dynamic core was developed at the U.S. National Center for Atmospheric Research (NCAR) in Boulder, CO. It is a non-hydrostatic mesoscale numerical weather prediction system originally designed to serve both operational forecasting and atmospheric research needs. The grid staggering for WRF is the Arakawa C-grid. The physics options used in this study include the new Kain–Fritsch cumulus parameterization (Kain, 2004), the WRF Single-Moment 5-class microphysics scheme (Hong *et al.*, 2004), the NCAR Community Atmosphere Model longwave and shortwave radiation (Collins *et al.*, 2004), the Noah Land Surface Model (Chen and Dudhia, 2001), and the YSU non-local boundary layer scheme (Hong *et al.*, 2006). The WRF domain is centred at 36.5°N, 102°E with 117 and 103 horizontal grid points in the zonal and meridional directions, respectively. The horizontal resolution is 50 km, and the Lambert conformal conic projection is used for the horizontal model coordinates with the standard parallel at 102°E (Figure 1(a)). The sea surface temperature (SST) in the simulation is adopted directly from the GCMs' output. For the land cover, a high-resolution data set from the WRF website is used, instead of the GCMs' land cover, which has a coarser resolution.

The RCM of RegCM4 (Giorgi *et al.*, 2012) was developed by the International Centre for Theoretical Physics (ICTP). It is a three-dimensional, σ -vertical coordinate, hydrostatic, compressible model with a dynamical core that is based on the fifth-generation mesoscale modelling system (MM5) (Grell *et al.*, 1994) from the Pennsylvania State University/NCAR. RegCM4 is run on an Arakawa B-grid in which wind and thermodynamical variables are horizontally staggered. The domain for RegCM4 is shown in Figure 1(b), which is centred at 36.5°N, 102°E, with a horizontal resolution of 50 km, and 124 (longitude) \times 112 (latitude) grid points. Even numbers of grids are adopted in the RegCM4 simulations to make it convenient for the segmentation of grids in the parallel computation, and thus get higher computation efficiency. The SUBEX scheme (Pal *et al.*, 2000) is applied for large-scale cloud and precipitation. The

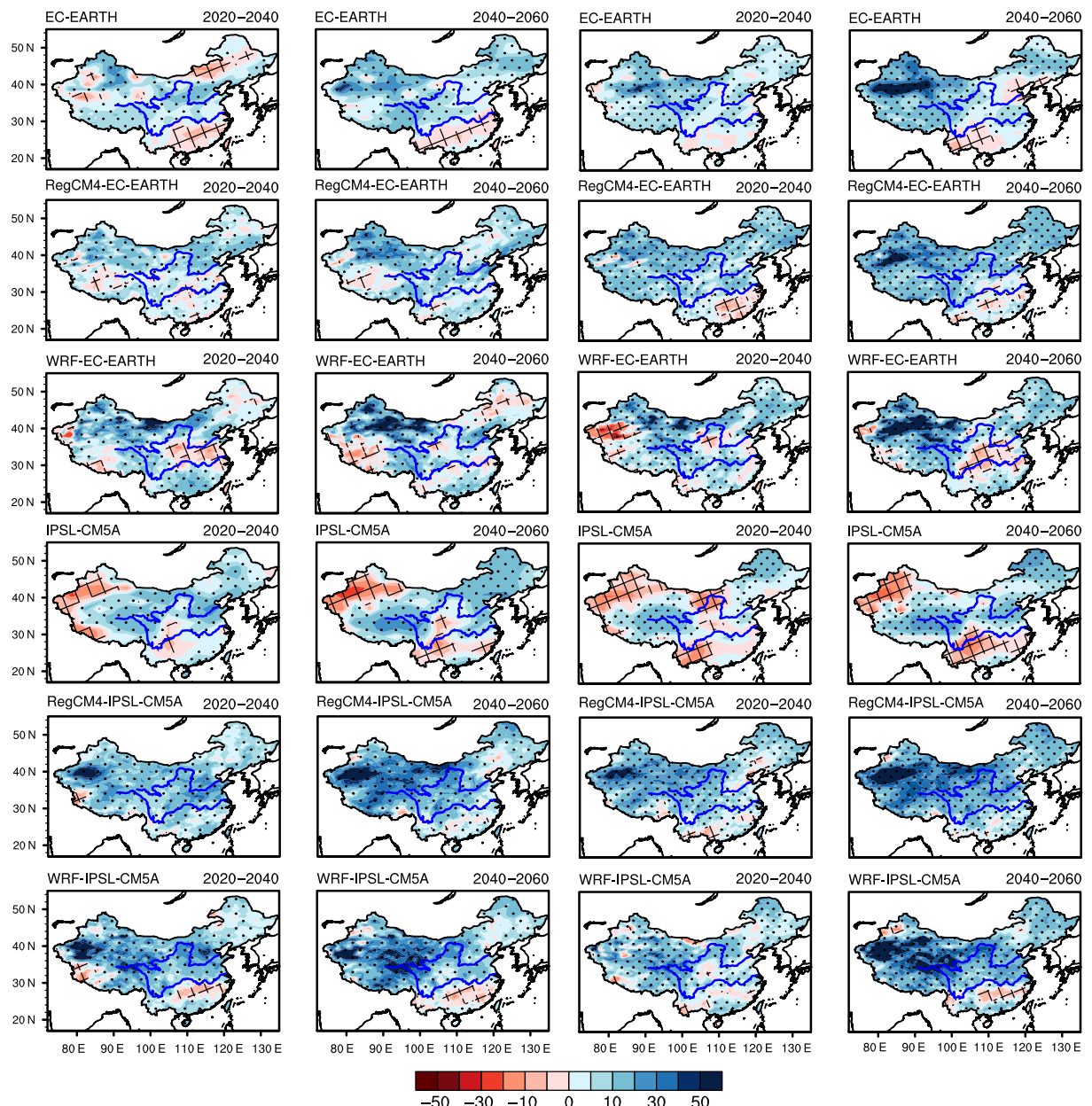


Figure 2. Spatial patterns of the annual mean precipitation changes relative to the present period of 1980–2000 under the RCP4.5 (first two columns) and RCP8.5 (last two columns) scenarios (unit: %). For each scenario, the changes over both periods of 2020–2040 and 2040–2060 are demonstrated. The areas with significant changes at 0.95 confidence level are indicated by black dots, and those with significant negative changes are indicated by cross lines.

Community Climate Model CCM3's radiation package for long and shortwave radiation (Kiehl *et al.*, 1998), the boundary layer physics Holtslag scheme (Holtslag and Boville, 1993), the MIT-Emanuel cumulus parameterization scheme (Emanuel and Zivkovic-Rothman, 1999) and CLM (community land model) land surface scheme (Lawrence *et al.*, 2011; Lawrence and Fisher, 2013) are used in this study. RegCM4 uses the same SST and land cover data set as WRF. The land surface scheme in RegCM4 would make some modification to the land cover data.

The downscalings with both RCMs are integrated continuously over 2019–2060, with the first year used as a spin-up that is not included in the analysis. Table 1 presents

a summary of the experimental design for both RCMs. The whole country is divided into eight sub-regions to analyse regional climate changes in the simulations, which is shown in Figure 1.

3. Result

3.1. Mean climatology

The projected changes of the annual mean precipitation in percentage over the two future periods of 2020–2040 and 2040–2060 relative to the present period of 1980–2000 are shown in Figure 2. The projections under the RCP4.5 and RCP8.5 scenarios are both demonstrated in the figure.

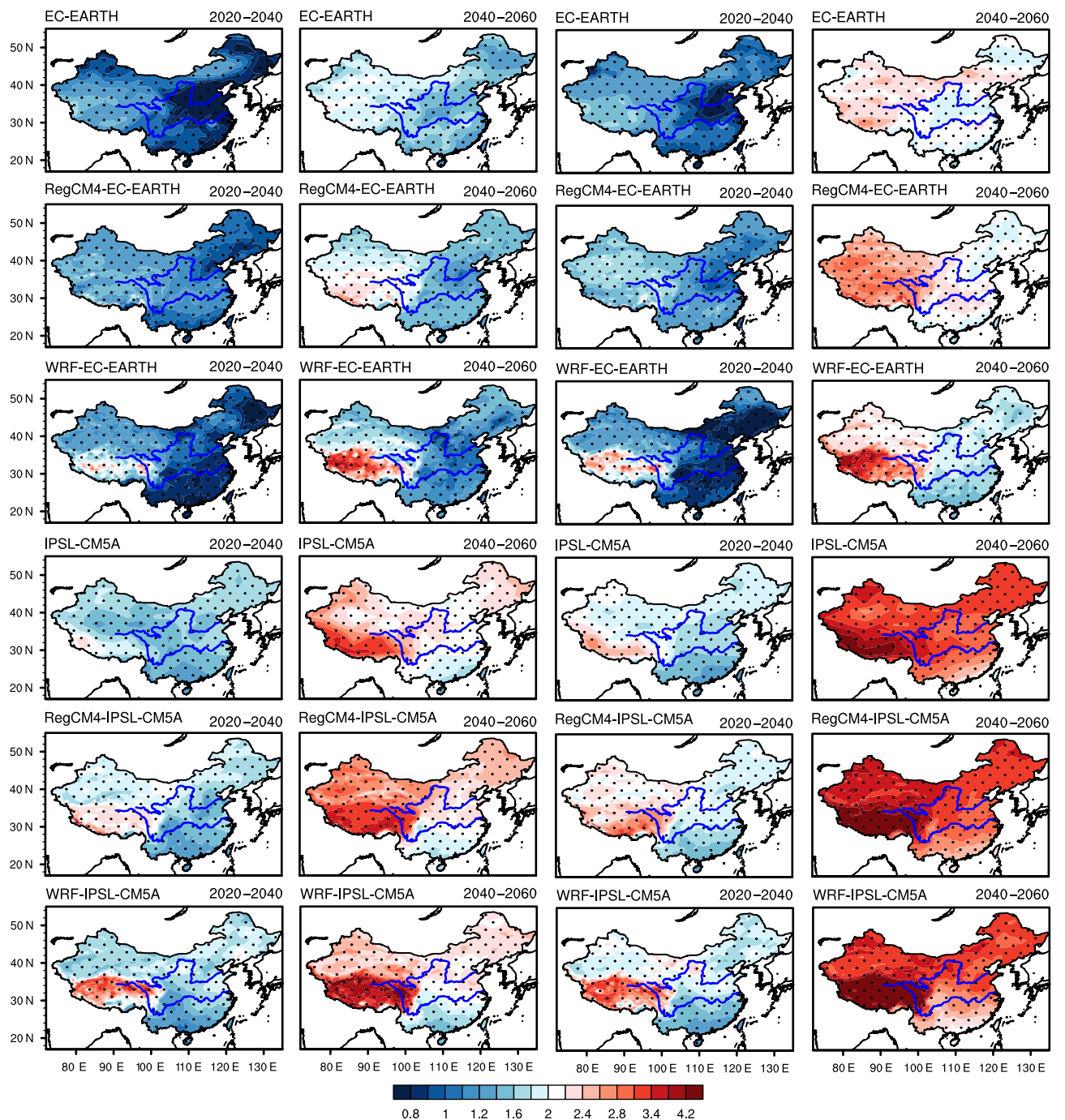


Figure 3. The same as Figure 2 but for surface air temperature (unit: °C).

It is shown that the projected changes in precipitation are significant at 0.95 confidence levels on most grids over China. Under the RCP4.5 scenario, the precipitation produced by EC-EARTH shows increase in North, eastern Northwest China, the Southern part of the Tibetan Plateau and some areas of Northwest China over the period of 2020–2040. The downscalings over EC-EARTH are greatly influenced by the GCM in most areas of the country, while the RCMs also modulate the patterns of the precipitation changes. The most significant adjustment made by the RCMs occurs over the Tibetan Plateau, with decrease of precipitation in most areas and increase on

the east edge of the plateau, and the RCMs produce more details since the finer presentation of regional topography and the mesoscale processes. In addition, the RCMs weaken the decrease of precipitation in Northeast China in EC-EARTH. Over the south-eastern part of China, RegCM4 projects decrease of precipitation, which is similar with the projection of EC-EARTH. However, the location of slight decrease of rainfall in the WRF projection exhibits northward shift compared to that in the RegCM4 model, and increase is projected along the southeast coast of China. By analysing the downscaled present-day climate, a strong rain band is found along the southeast shore

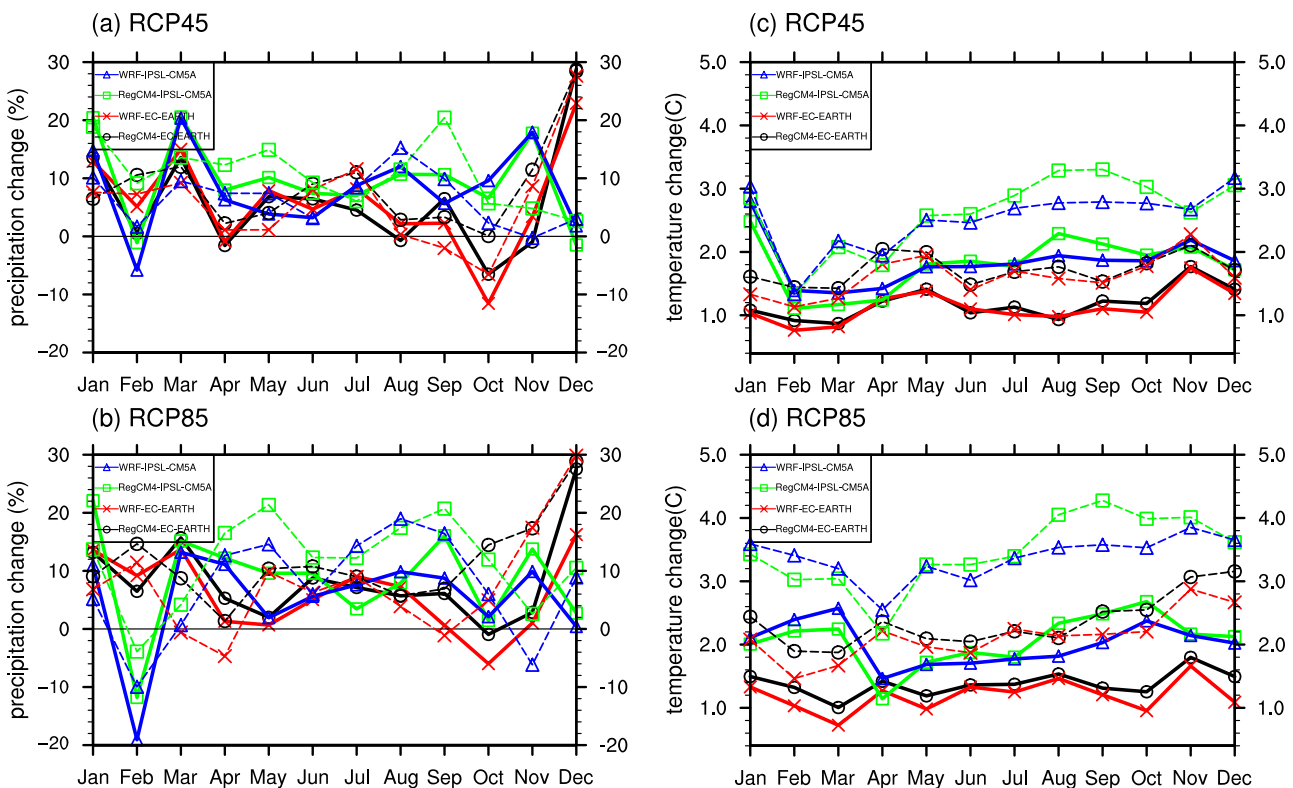


Figure 4. Annual cycles of the changes of precipitation (a, b; unit: %) and temperature (c, d; unit: $^{\circ}\text{C}$) under the RCP4.5 and RCP8.5 scenarios. The solid lines represent the changes during 2020–2040 and dashed lines for 2040–2060.

in the WRF downscaling, which may be further intensified in the future and results in increase of precipitation over this area.

The precipitation change produced by IPSL-CM5A shows differences with that in EC-EARTH in Northwest China and over the Tibetan Plateau, with increase over most areas of the Tibetan Plateau and decrease in most part of Northwest China. The downscalings over IPSL-CM5A project greater increase of precipitation occupying larger areas than the GCM, with the greatest values over 50% in the Tarim Basin, and decrease only occurs in some small areas over the Tibetan Plateau, Northeast and South China. The downscalings over IPSL-CM5A produce stronger increases of precipitation while similar spatial distributions compared with those over EC-EARTH. Over the south-eastern part of China, the northward shift of precipitation decrease and the increase of rainfall along the southeast coast are also projected in the WRF downscaling over IPSL-CM5A.

In the simulations of the annual mean precipitation for the present climate (Hui *et al.*, 2018), the RCMs could bring out added values to the GCM of EC-EARTH over the Tibetan Plateau and Northeast China, and the RCMs also significantly improved the performance of IPSL-CM5A in most regions of China. So, the modifications made by the downscalings for the precipitation changes can be valuable. In the period of 2040–2060, the increase of precipitation further intensifies compared with that during 2020–2040, and the RCMs strengthen the wetness in the GCMs through downscalings. Under the RCP8.5 scenario

(last two columns), the projected changes of precipitation over both time periods of 2020–2040 and 2040–2060 present similar patterns with those under the RCP4.5 scenario, respectively, and the increases of precipitation have larger spatial coverage and higher intensity than those under the RCP4.5 scenario. Over the period of 2040–2060, decrease of precipitation is only found in Southeast, South and Southwest China and some scattered areas in Northeast and Northwest China.

The changes of the annual mean surface air temperature are shown in Figure 3. The temperature is projected to increase with time over the whole domain under both scenarios, which is significant at 0.95 confidence level on all the grids. The projected climate tends to be much warmer under the RCP8.5 scenario, in which greenhouse gas emissions continue to rise throughout the 21st century (last two columns). The changes of temperature under different scenarios exhibit similar spatial patterns, with the largest increase occurring on the Tibetan Plateau and the weakest increase in Southeast and South China. The severe warming in the regions with high altitude like the Tibetan Plateau has been attributed to the snow albedo feedback by Hui *et al.* (2014).

Under each scenario, the GCM of IPSL-CM5A produces much warmer climate in the future than EC-EARTH. The downscalings demonstrate very similar patterns and magnitudes of temperature changes with those in the driving GCMs, except that the climate warming over the Tibetan Plateau is intensified by the RCMs and more regional details are generated in the downscalings.

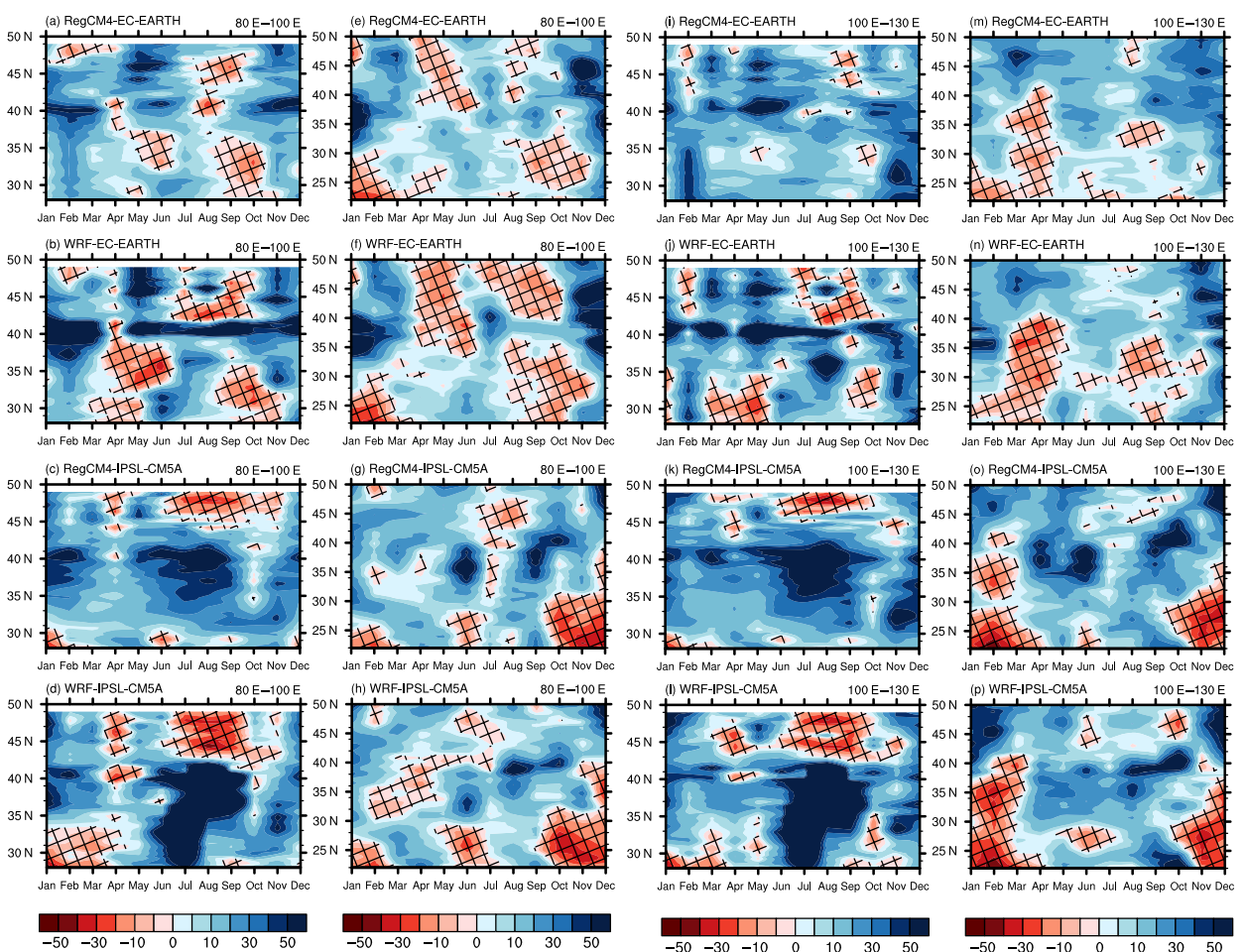


Figure 5. Latitude-month cross-sections of the precipitation changes averaged between 80° – 100° E and 100° – 130° E under the RCP4.5 (a–d, e–h) and RCP8.5 (i–l, m–p) scenarios (unit: %). The cross lines indicate the areas with negative changes.

Although the two RCMs produced larger biases than the GCMs for the magnitude of the annual mean temperature over the present period, the RCMs succeeded in producing more realistic spatial patterns of temperature than the GCMs for their higher resolutions (Hui *et al.*, 2018). And the systematic errors of the RCMs can be eliminated by subtracting the present climate from the future climate. So, the downscaled temperature in the future can provide valuable information for the fight over climate change. Comparing the downscalings with the two RCMs, the projected warming by WRF is weaker than that in RegCM4 over most areas of China. As shown by Hui *et al.* (2018), WRF produces colder temperature than RegCM4 for the present climate, with the simulation by RegCM4 more consistent with the observation. The cold bias in WRF may get stronger in the future, as a result, weaker warming is projected in the WRF downscalings.

3.2. Annual cycle

The 20-year averaged seasonal cycles of downscaled climate changes over China over both periods of 2020–2040 and 2040–2060 are shown in Figure 4. The solid and dashed lines represent the climate changes in the period of

2020–2040 and 2040–2060, respectively. Increasing precipitations are projected in all the downscalings in most months except in February and October under the RCP4.5 scenario (Figure 4(a)). The greatest relative increase larger than 20% occurs in December in the downscalings of EC-EARTH. But in the IPSL-CM5A downscalings, the RCMs project much lighter increase close to 0% in December. In January and March, large positive changes are projected in all the downscalings, which are ranging from 8 to 20%. In most months, the downscalings over IPSL-CM5A project more precipitation than the EC-EARTH downscalings. Comparing the precipitation changes in the two future time slices, it is found that the monthly precipitations will further increase in the period of 2040–2060, especially in April, May, August and September. Under the RCP8.5 scenario (Figure 4(b)), the monthly precipitation changes show similar seasonal cycles to those under the RCP4.5 scenario, but the inter-month fluctuations are much stronger, indicating stronger seasonality with high-emission rate. Figure 4(c) shows that, under the RCP4.5 scenario, the warming during 2020–2040 is ranging from 1.0 to 2.0 °C in different experiments, with stronger intensity in the later months of the year. The downscalings driven by IPSL-CM5A produce stronger

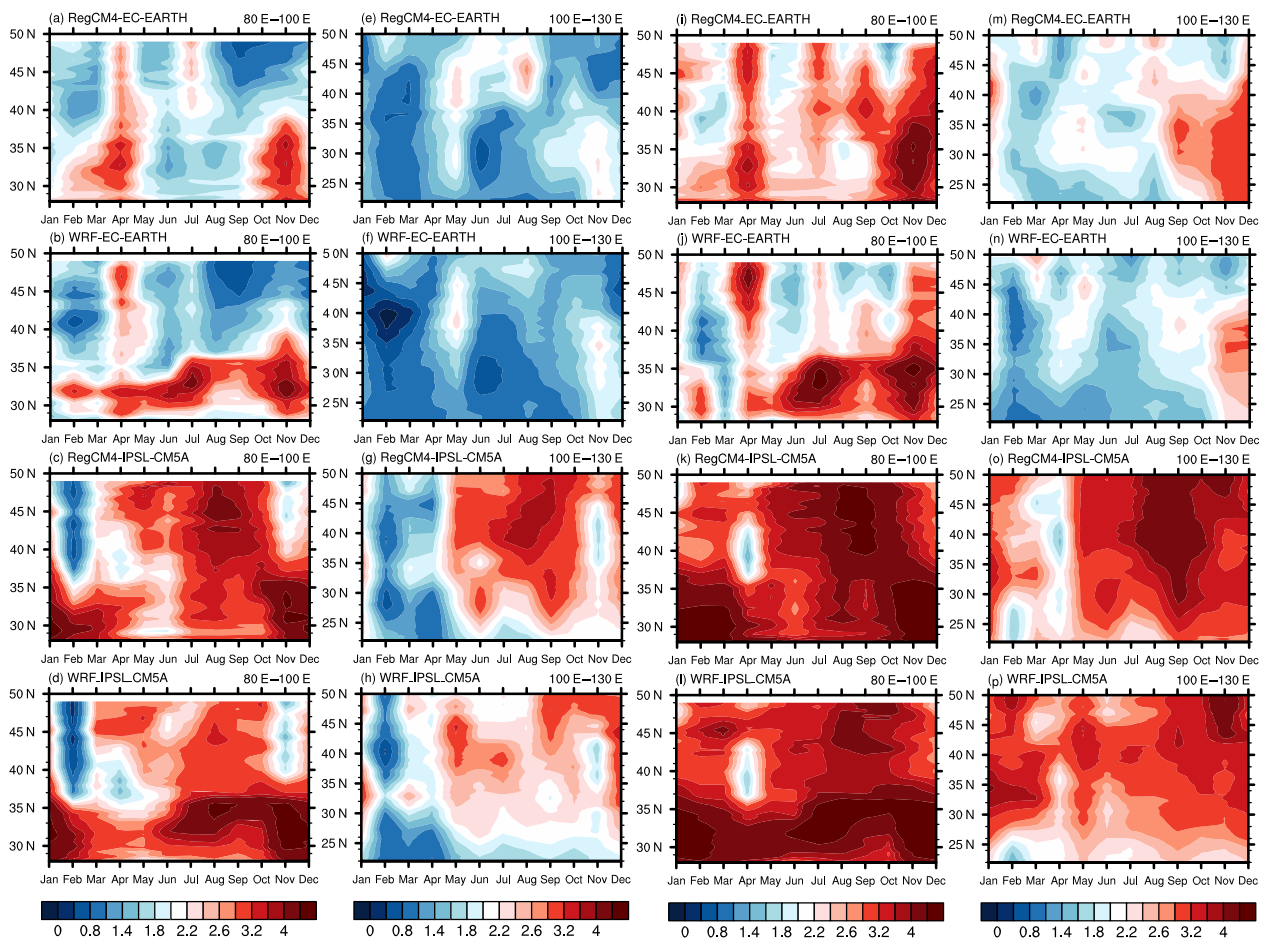


Figure 6. The same as Figure 5 but for the surface air temperature.

warming, which is about 1 °C higher than the warming down-scaled from EC-EARTH. Over the period of 2040–2060, the monthly temperatures get higher than those during 2020–2040 through the whole year, with further increases of about 1 °C in the IPSL-CM5A driving simulations and 0.6 °C in the EC-EARTH driving projections. Higher emission scenario of RCP8.5 does not induce stronger warming in case of regional averaged monthly temperature during 2020–2040 (Figure 4(d)). However, remarkable warming can be up to 4 °C in the latter half of the year over the period of 2040–2060 from RCP8.5.

The climate changes in different areas of China exhibit different features, and the latitude-month cross-sections of climate changes averaged over the western (80°–100°E) and eastern (100°–130°E) parts of China during 2040–2060 are given in Figures 5 and 6. The two parts are divided along the eastern edge of the Tibetan Plateau. The impacts of GCMs are evident in the precipitation projections, suggesting that the large-scale circulation and water transport can be dominating in the future moisture and precipitation changes. On the other hand, the model physics of the RCMs cannot be ignored in deciding the intensity of the precipitation climatology and its variations.

Under the RCP4.5 scenario, the EC-EARTH down-scalings project wetter winter and summer, while drier spring

and autumn below 42°N in the western part (Figures 5(a) and (b)), and the precipitation at high latitudes would increase in early summer and early winter. The increase of precipitation along 40°N, where the Tarim Basin is located, is the most significant. The down-scalings of IPSL-CM5A produce similar patterns and variations of precipitation changes with those in the EC-EARTH down-scalings, while project stronger increases of precipitation below 42°N and stronger decreases above it (Figures 5(c) and (d)). In the eastern part, wetter winter and summer while drier spring and autumn are projected by the EC-EARTH down-scalings in almost all the low latitude and high-latitude regions (Figures 5(e) and (f)), which are similar with the projections in the western part. However, the monthly precipitation changes in the IPSL-CM5A down-scalings present different patterns, with less precipitation in summer and winter in low latitudes and drier summer above 40°N (Figures 5(g) and (h)). The monthly precipitations at different latitudes would experience similar patterns of changes under the RCP8.5 scenario with those under the RCP4.5 scenario, but there also exists some differences. In general, the projected precipitations under the RCP8.5 scenario would increase in more regions as well as in more months.

Figure 6 shows the latitude-month cross sections of temperature changes. Warming is expected at all the

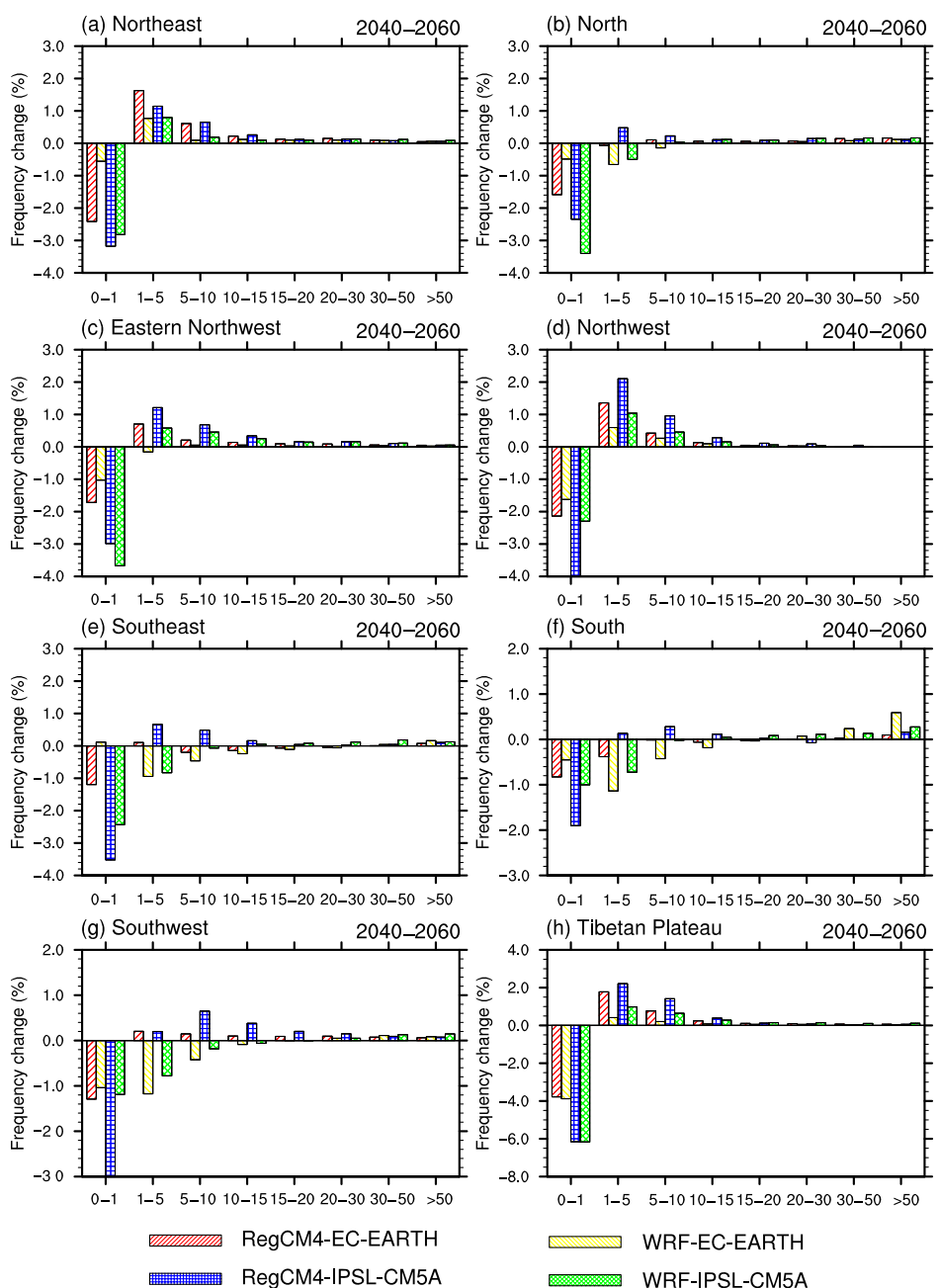


Figure 7. Changes of the probability distribution functions (PDFs) of daily precipitation in different sub-regions over China over the period of 2040–2060 under the RCP8.5 scenario. (a) Northeast, (b) North, (c) Eastern Northwest, (d) Northwest, (e) Southeast, (f) South, (g) Southwest and (h) Tibetan Plateau.

latitudes through the whole year in both western and eastern parts. In the downscalings under the RCP4.5 scenario for the western part (Figures 6(a)–(d)), the greatest warming appears around 30°N where the Tibetan Plateau is located. The temperature projections are highly dependent on the forcing fields from the GCMs, with the downscalings over IPSL-CM5A producing more intensive warming. The RCMs also influence the projections when downscaling the same GCM, especially in summer and autumn. In general, WRF produces more intensive warming than RegCM4 on the Tibetan Plateau while weaker warming over the other areas. In the eastern part (Figures 6(e)–(h)), the temperature increases in the first

4 months of the year are relatively weaker in all the four projections. The greatest warming is projected in May, as well as in summer and early autumn at high latitudes. The downscalings over IPSL-CM5A project much greater warming than those over EC-EARTH (Figures 6(c) and (d)), with the largest temperature increase around 4–5 °C occurring between 40 and 45°N in August in the RegCM4 projection (Figure 6(c)). Under the RCP8.5 scenario, the monthly temperatures show much stronger warming in both eastern and western parts (Figures 6(i)–(p)). The temperature rise projected in the IPSL-CM5A driving simulations is above 2 °C at almost all the latitudes all through the year (Figures 6(k), (l), (o) and (p)).

Table 2. Definitions of extreme precipitation and temperature indices.

Variables	Definition	Units
CDD	Maximum number of consecutive days with Precipitation <1 mm	days
CWD	Maximum number of consecutive days with Precipitation >1 mm	days
R \times 5	Annual maximum consecutive 5-day precipitation	mm
R95	Annual total precipitation when Pre. >95th percentile	mm
TXx	Annual maximum value of daily max temperature	°C
TNn	Annual minimum value of daily min temperature	°C
WSDI	Annual count when at least six consecutive days of max temperature >90th percentile	days
CSDI	Annual count when at least six consecutive days of min temperature <10th percentile	days

3.3. Probability density functions

The changes of probability density functions (PDFs) for precipitation during 2040–2060 under the RCP8.5 scenario are illustrated in Figure 7. The frequency of drizzle rain with intensity less than 1 mm day^{-1} is projected to decrease in all the sub-regions by most simulations, and the strongest decrease up to 6% occurs in the Tibetan Plateau. The light rain of $1\text{--}5 \text{ mm day}^{-1}$ and $5\text{--}10 \text{ mm day}^{-1}$ is expected to be more frequent in the future, except in the three Southern sub-regions where decreases of light rain ($1\text{--}10 \text{ mm day}^{-1}$) frequency are projected in some simulations (Figures 7(e)–(g)). For the moderate to heavy rain ($10\text{--}50 \text{ mm day}^{-1}$), slight increases of frequency ranging from 0 to 0.1% are projected in all the sub-regions, and South China would experience more moderate to heavy rainfall with its frequency increasing by up to 0.4% (Figure 7(f)). This region would suffer from more severe storms under the high-emission scenario in the future by about 0–0.6%. The decrease of light rain and increase of heavy precipitation was also indicated in China by Bao *et al.* (2015) and in other areas over the world (Christensen and Christensen, 2007; Jacob, 2014). The downscalings over EC-EARTH project weaker changes for the PDFs of precipitation, and WRF shows even weaker changes than RegCM4, which is especially evident in the four Northern regions (Figures 7(a)–(d)). The changes in the PDFs of precipitation under the RCP4.5 scenario (figure not shown) present very similar patterns with those under the RCP8.5 scenario, except that the intensities of the changes are much weaker.

3.4. Extreme indices

It has been validated in Part I of this research that the four downscalings can reasonably produce the eight extreme indices, which are defined in Table 2, for control climate of 1980–2000. The responses of extreme climate to warmer

mean climate are investigated in this work. Since the changes of extreme precipitation and temperature under the RCP4.5 display similar patterns to those under the RCP8.5 scenario and have smaller magnitudes, this work only analyses the changes under the RCP8.5 scenario. The changes of extreme precipitation indices over the period of 2040–2060 are presented in Figure 8. Under the warming climate conditions, the convective dry days (CDD) is projected to decrease in the western part of China and Northeast China (Figures 8(a)–(d)), and the greatest decreases above 20 days appear in the Tarim Basin, since the more abundant precipitation in the future. In the south-eastern part of China, the CDD increases by mostly less than 8 days. The sub-region averages show decreases of CDD in North parts of China and the Tibetan Plateau, and the rest of the country might experience increasing CDD. For the wet extreme indices of convective wet days (CWD), maximum 5-day precipitation amount (R \times 5) and very wet days (R95), increases are projected over most regions of China, only with some patched areas of weak decreases (Figures 8(e)–(p)). The largest increases about 5 days of the CWD are projected on the southeast edge of the Tibetan Plateau in all the simulations (Figures 8(e)–(h)). The future changes of the CWD are more sensitive to the choice of RCMs than the driving GCMs, as spatial similarity can be found between the projections from the same RCM. Meanwhile, the RegCM4 projects much stronger increase of CWD, especially in Southeast, South, Southwest China and the Tibetan Plateau (Figures 8(e)–(h), Figure 9(b)). Hui *et al.* (2018) indicated that RegCM4 produced greater CWD than WRF when driven by the same GCM for the present climate, especially in the south-eastern part of China and over the Tibetan Plateau. And as time goes on, the CWD projected by RegCM4 may get even larger, resulting in greater increases than those in the WRF projections. Comparing the downscalings driven by different GCMs, the projections nested within IPSL-CM5A tend to produce greater increase of CWD than those nested within EC-EARTH. The changes of R \times 5 and R95 show very similar spatial patterns (Figures 8(i)–(l) and (m)–(p)), and significant increases are projected over almost the whole country except in some scattered areas. The increases of R \times 5 and R95 are both the weakest in Northwest China, with magnitude of 0–10 mm and 0–60 mm, respectively (Figures 9(c) and (d)). The strongest increases of R \times 5 and R95 are generated in South China, which are up to 60 and >240 mm in the WRF downscaling over EC-EARTH. Similar to the CWD, the increases of R \times 5 and R95 are generally greater in the IPSL-CM5A downscalings (Figures 8(k)–(l) and (o)–(p)). The projections for extreme precipitation indices are consistent with Qin and Xie (2016), who projected more wet extremes in most areas, and less dry extremes in arid and semiarid areas in Northwest China.

The changes of extreme temperatures under the RCP8.5 scenario are shown in Figures 10 and 11. The driving fields from different GCMs exert great impact on the projections of all the four indices, with more significant changes in the IPSL-CM5A driven simulations.

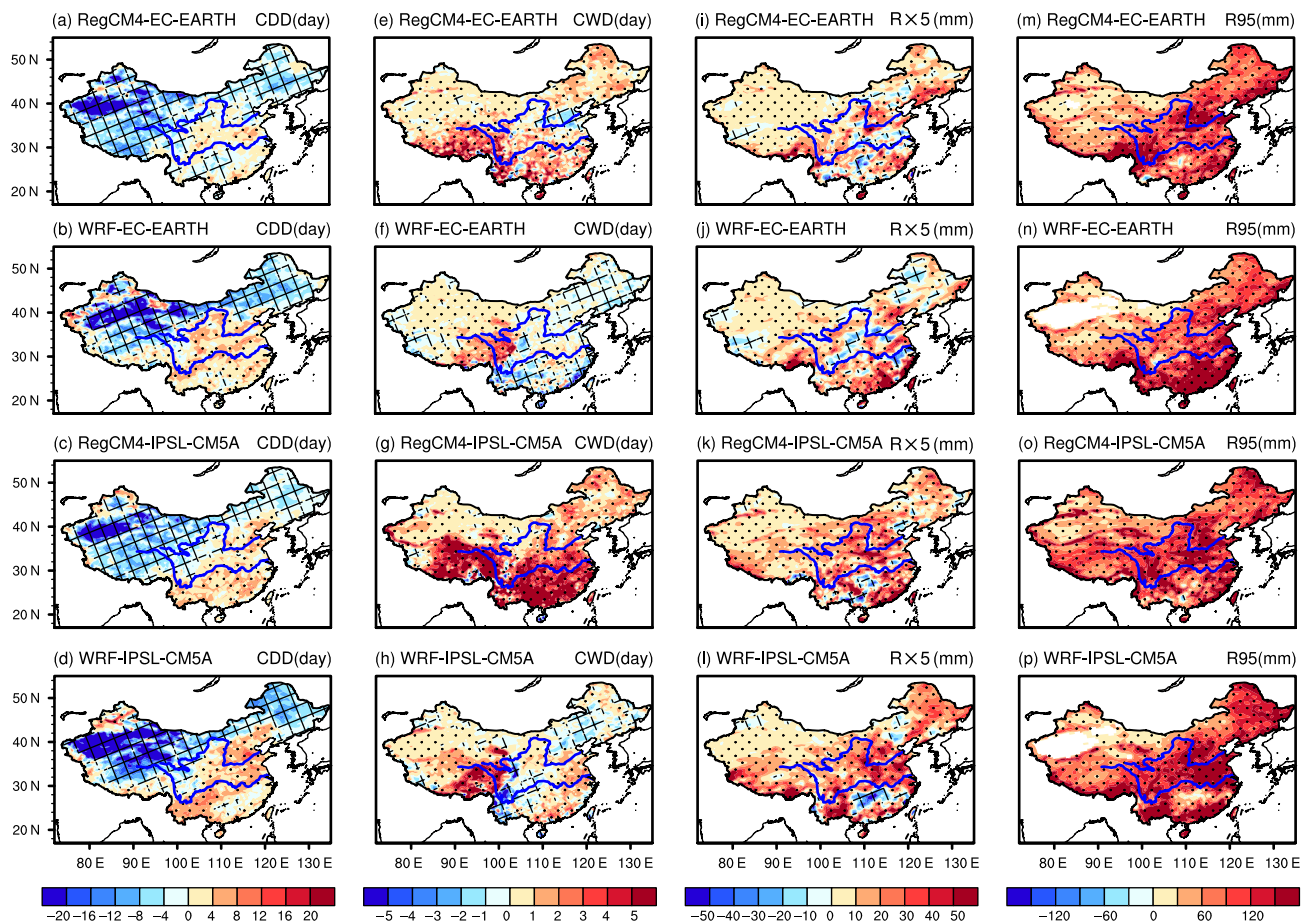


Figure 8. Spatial patterns of changes in the extreme precipitation indices of CDD (a–d), CWD (e–h), Rx5 (i–l) and R95 (m–p) under the RCP8.5 scenario. The results from different RCM simulations are demonstrated from top to bottom. The areas with significant positive changes at 0.95 confidence level are indicated with black dots, and those with significant negative changes are indicated with cross lines.

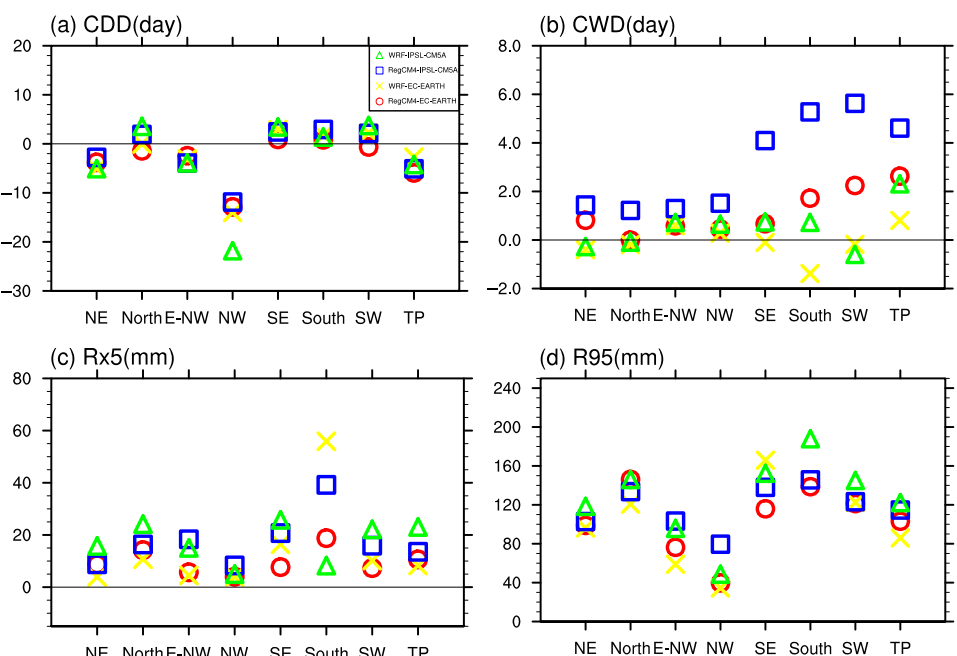


Figure 9. Changes of the extreme precipitation indices of CDD (a), CWD (b), Rx5 (c) and R95 (d) averaged in the eight sub-regions in different RCM simulations under the RCP8.5 scenario.

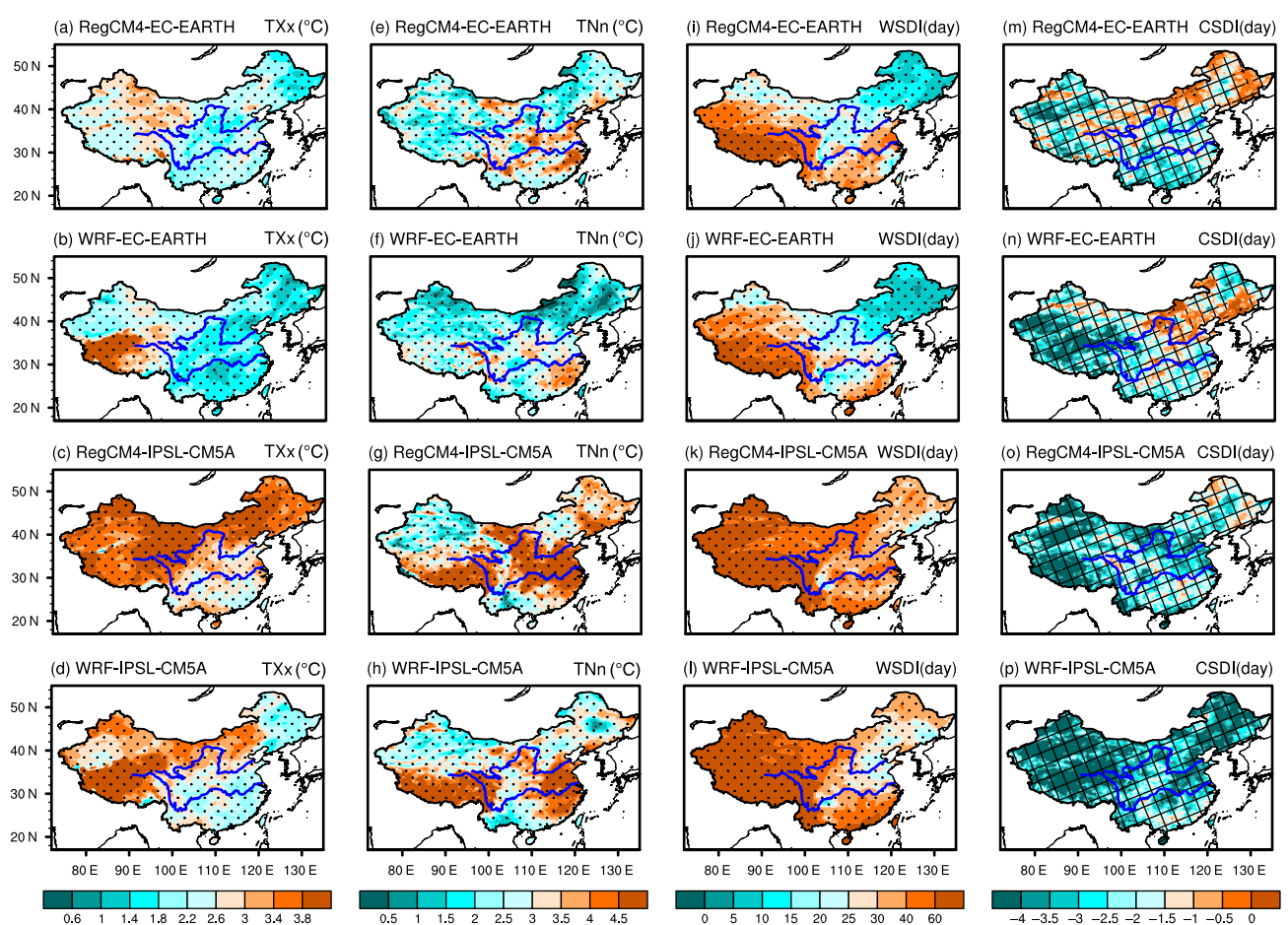


Figure 10. The same as Figure 8 but for the extreme temperature indices of TXx (a–d), TNn (e–h), WSDI (i–l), and CSDI (m–p).

The max Tmax (TXx) and min Tmin (TNn) are both projected to increase over the whole domain, and the increases produced by RegCM4 are even more significant over most areas. The increase of TXx is relatively stronger in the north-western areas in each simulation (Figures 10(a)–(d)), with the largest value above 4 °C occurring on the Tibetan Plateau in the IPSL-CM5A downscalings (Figures 10(c) and (d)). Figure 11(a) presents the regional mean change of TXx in different sub-regions, which shows the largest increase over the Tibetan Plateau reaching to 5.5 °C in the WRF-IPSL-CM5A simulation. The increases of TXx in the Northern sub-regions such as Northeast, North, eastern Northwest and Northwest China are ranging between 2 and 4 °C, while they are below 1 °C in Southeast, South and Southwest China. As for the TNn (Figures 10(e)–(h)), the largest increase occurs in Southeast China and the Tibetan Plateau, especially in the IPSL-CM5A driven simulations. Figure 11(b) shows that the averaging increases of TNn in Southeast China and the Tibetan Plateau can reach to 5.5 °C in the downscalings over IPSL-CM5A, while Northwest China would experience weak increase of TNn. The changes of warm spell duration indicator (WSDI) and cold spell duration indicator (CSDI) demonstrate the similar patterns but opposite signs, and the greatest increase of WSDI and decrease of

CSDI are both found over the Tibetan Plateau. In the downscalings over IPSL-CM5A, the regional averaged increase of WSDI is over 100 days over the Tibetan Plateau, and the CSDI decrease is between –4 and –5 days over this region(Figures 11(c) and (d)). The changes of WSDI and CSDI are relatively weak in Northeast, North and eastern Northwest China in each simulation.

3.5. Possible reasons for changes in mean and extreme precipitation

The possible factors controlling the change of mean precipitation are first investigated by analysing the changes of total water vapour flux and divergence at 850 hPa (Figure 12). As shown in Figure 2, the annual mean precipitation is expected to increase in most regions of China in the downscalings over the period of 2040–2060 under the RCP8.5 scenario, especially in the downscalings over IPSL-CM5A. Decrease is projected mainly in the south-eastern part of China. Figure 12 indicates that, with the higher temperature in the future, the water content increases in the atmosphere, leading to increasing water vapour flux over almost whole China. The increases of water vapour flux are much greater in the IPSL-CM5A downscalings, resulting in larger increases of precipitation. In Southeast, South and Southwest China, the increases of water vapour flux have lower values and even

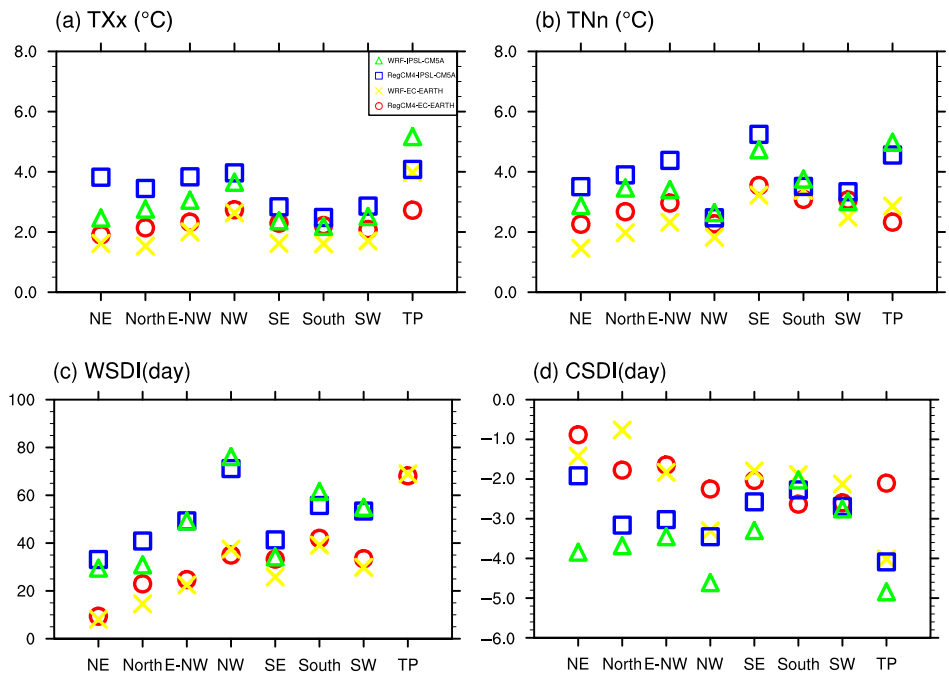


Figure 11. The same as Figure 9 but for the extreme temperature indices of TXx (a), TNn (b), WSDI (c) and CSDI (d).

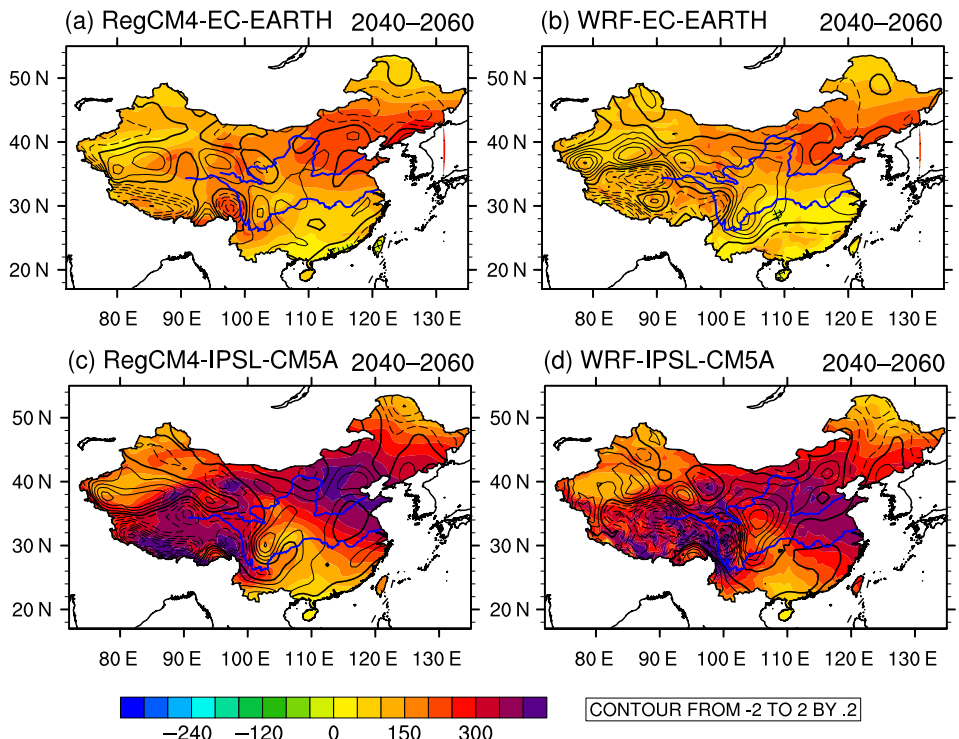


Figure 12. Changes of the total water vapour flux integrated from 1000 to 200 hPa (shading, unit: $\text{g} \cdot \text{s} \text{kg}^{-1}$) and the divergence at 850 hPa (contour, unit: 10^{-6}s^{-1}) over the period of 2040–2060 under the RCP8.5 scenario. The cross lines indicate the areas with negative changes of water vapor flux.

weak decreases are projected. What is more, the wind vectors at 850 hPa would experience divergent changes in these regions. As a result, these areas would go through drought in the future. It can be noted that, the WRF downscalings produce relatively larger increases of water vapour flux than RegCM4 along the southeast coast of China, especially when driven by EC-EARTH, which can

explain the rainfall increases over this region in the WRF downscalings shown in Figure 2. In most areas of Northeast China and the Tibetan Plateau, both the significant increases of water vapour flux and the convergent changes of low-level wind vectors contribute to the increases of precipitation.

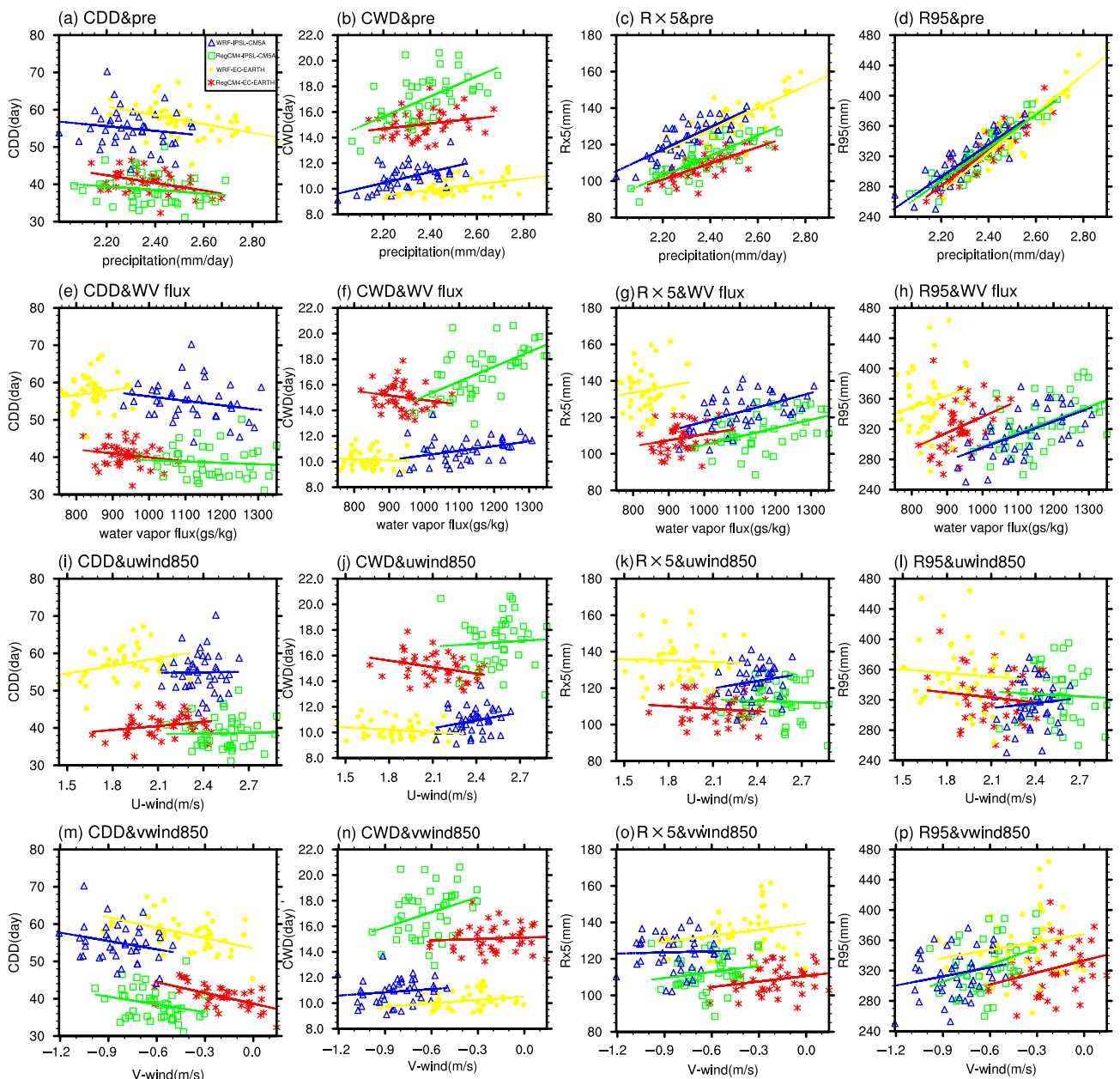


Figure 13. Scatter diagrams of the extreme precipitation indices CDD (a–d), CWD (e–h), Rx5 (i–l) and R95 (m–p) against the annual mean precipitation, total water vapour flux integrated between 1000–200 hPa, zonal and meridional winds as well as the linear regressions under the RCP8.5 scenario. The variables cover the period of 2020–2060 and are averaged over China.

Figure 13 shows the scatter diagrams of extreme precipitation indices against various climate variables, and the correlation analysis is exhibited in Figure 14. As shown in Figures 13(a)–(d), all the four extreme precipitation indices are sensitive to annual mean precipitation. The dry index of CDD is negatively correlated with precipitation and the three wet indices are positively correlated with it. Figure 14 shows that CDD is more dependent on winter and autumn precipitation because of the fewer occurrences of rainy days in these two seasons. On the other hand, the wet extreme indices present higher correlation with precipitation in summer. High correlation is also found between the extreme indices and the seasonal and annual water vapour flux (Figures 13(e)–(h) and 14), because

the close relationship between precipitation and moisture. However, the correlations are relatively weaker than those between the wet indices and precipitation. The zonal wind at 850 hPa shows little impact on the extreme precipitation indices in all the simulations, but to some degree the meridional wind can influence the indices (Figures 13(m)–(p)). Figure 14 shows that the dry index of CDD has negative correlation with winter, autumn and annual mean meridional wind. And positive correlations are found between the three wet indices and the meridional wind in summer as well as when annually averaged. It, therefore, can be concluded that, when summer monsoon gets stronger (positive v-wind increases), more moisture would be transported to China which could lead to more summer precipitation, as

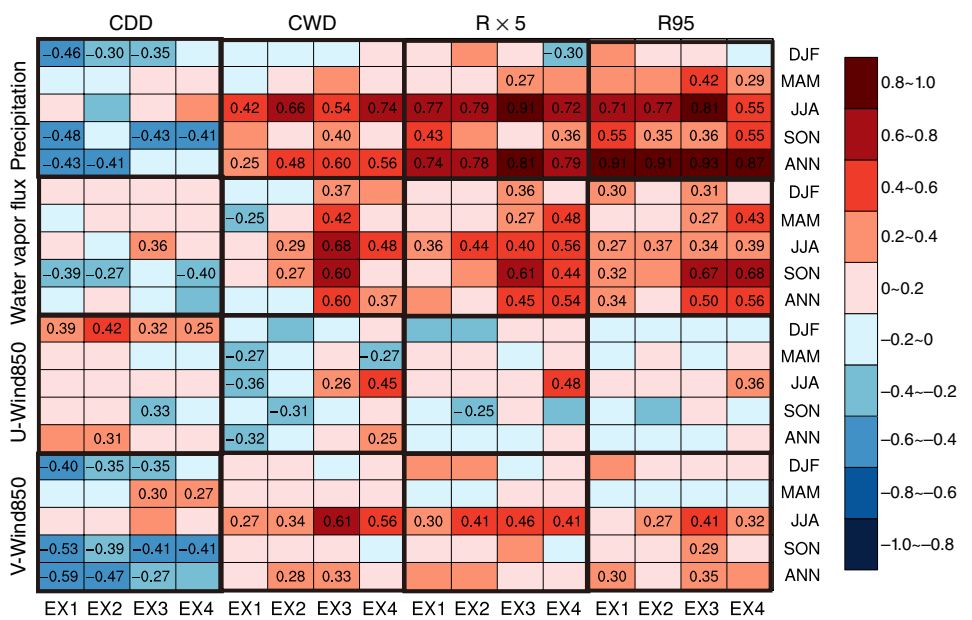


Figure 14. The correlation coefficients between the extreme precipitation indices and the climate variables such as precipitation, total water vapour flux integrated between 1000–200 hPa, zonal wind and meridional wind at 850 hPa under the RCP8.5 scenario. The correlation coefficients significant at 0.1 confidence level are printed. EX1-4 represent the simulations of RegCM4-EC-EARTH, WRF-EC-EARTH, RegCM4-IPSL-CM5A, and WRF-IPSL-CM5A.

a result, the wet extreme indices get to increase. On the other hand, when winter monsoon becomes weaker (negative v-wind increases), dry condition could be suppressed and CDD gets to decrease. This proposed mechanism is the same with that for the projected rainfall changes with a regional ocean–atmosphere coupled model by Zou and Zhou (2016).

4. Conclusion

In this study, the changes in mean and extreme climate in China are detected with the RCMs of WRF and RegCM4, by downscaling the simulations from EC-EARTH and IPSL-CM5A to regional scale. The climate change during 2020–2060 is projected under the RCP4.5 and RCP8.5 scenarios after evaluating the RCMs' ability in Part I of this research. Significantly changes in both mean and extreme climate are detected in the future. Generally, the patterns of climate change are insensitive to the RCP scenarios, with stronger changes under the RCP8.5 scenario.

The projected changes of mean climate are firstly investigated in the work. Increase of annual mean precipitation is projected by the downscalings in most regions of China, such as Northwest, eastern Northwest, North China, partially Northeast China, and the east part of the Tibetan Plateau, with the strongest relative increase in the Tarim Basin. The wetness in these regions tend to get greater over time. Annual cycles of precipitation changes indicate that the increase of annual mean precipitation is mainly owing to the increase in summer and winter. Slight decrease of precipitation would mainly occur in the regions with abundant rainfall such as Southeast, Southwest and South China. The frequency of drizzle rain is projected to

decrease with the greatest change over the Tibetan Plateau, while the moderate to heavy rainfall as well as the storm would occur more frequently in the future. The annual mean temperature would increase over the whole domain with the greatest increase occurring on the Tibetan Plateau.

The changes in mean climate highly depend on the driving GCMs, and the downscalings of IPSL-CM5A produce wetter and warmer climate as well as greater change in the PDFs in the future. The RCMs also modulate the patterns of climate changes and generate more regional details. Since the RCMs can bring out added values to the GCMs (Hui *et al.*, 2018), the modifications made by the downscalings for the climate changes can be valuable. Comparing the two RCMs, WRF produces stronger drought as well as wetness than RegCM4, but weaker changes in the PDFs are produced by WRF. What is more, WRF projects stronger warming over the Tibetan Plateau in summer and autumn, and weaker warming over the other areas in these two seasons.

Afterwards, we detect the changes in extreme precipitation and temperature. Increase of the dry extreme index such as CDD is found in the wet areas with abundant precipitation, such as Southeast, Southwest and South China, while decrease is detected in the arid and semiarid regions, especially in Northwest China. The wet extreme indices of CWD, Rx5 and R95 would increase in most regions, only with some patched areas of weak decrease. The wet extremes in the wet areas and over the Tibetan Plateau would be more sensitive to climate change. It should be noted that the decrease of CDD and increase of wet extremes in the south-eastern areas indicate the more consecutive rainy and dry days, as well as more extreme rainfall events. The downscalings of IPSL-CM5A tend to create larger wet extremes than EC-EARTH in most

regions, while only the change in CWD is sensitive to RCMs with stronger increase exhibited by the RegCM4. Considering the change of extreme temperature, increase is projected for TXx, TNn and WSDI over the whole country while decrease is found in CSDI. Among the different sub-regions, the Tibetan Plateau would undergo the strongest change in all the four indices. The changes of temperature extremes are also sensitive to the driving fields, with more intensive change in the IPSL-CM5A downscalings, and RegCM4 produces even more significant changes of TXx and TNn.

Finally, the possible mechanism for change of mean precipitation and the connection between extreme climate and changing mean climate are investigated. The combined contributions of convergent change of wind vector at 850 hPa and increase of total water vapour flux lead to increase of precipitation. The extreme precipitation is highly related with the mean precipitation, water vapour flux and meridional wind. When the summer monsoon gets stronger in the future, more moisture would be transported to China which could lead to more summer precipitation, as a result, the wet extreme indices get to increase. On the other hand, the winter monsoon becomes weaker and the dry condition in winter could be suppressed, which leads to decrease of CDD.

Acknowledgements

The work is jointly funded by the Ministry of Science and Technology of China (2016YFA0600303) and the National Natural Science Foundation of China (41375075). We thank the ECMWF and the Institute Pierre Simon Laplace for providing the EC-EARTH and IPSL-CM5A model output that we used to drive WRF and RegCM4. The authors also appreciate the support of the NCAR and ICTP for providing RCMs that are used in this study.

References

- Alexander L, Zhang X, Peterson T, Caesar J, Gleason B, Klein Tank A, Haylock M, Collins D, Trewin B, FR, AT, Ambenje P, Rupa Kumar K, Revadekar J, Griffiths G. 2006. Global observed changes in daily climate extremes of temperature and precipitation. *J. Geophys. Res.* **111**: D05109. <https://doi.org/10.1029/2005JD006290>.
- Andrys J, Kala J, Lyons TJ. 2016. Regional climate projections of mean and extreme climate for the southwest of Western Australia (1970–1999 compared to 2030–2059). *Clim. Dyn.* **48**: 1723–1747. <https://doi.org/10.1007/s00382-016-3169-5>.
- Bao Q. 2012. Projected changes in Asian summer monsoon in RCP scenarios of CMIP5. *Atmos. Oceanic Sci. Lett.* **5**: 43–48.
- Bao J, Feng J, Wang Y. 2015. Dynamical downscaling simulation and future projection of precipitation over China. *J. Geophys. Res. Atmos.* **120**(16): 8227–8243. <https://doi.org/10.1002/2015jd023275>.
- Chen F, Dudhia J. 2001. Coupling an advanced land surface–hydrology model with the Penn State–NCAR MM5 modeling system. Part I: model implementation and sensitivity. *Mon. Weather Rev.* **129**: 569–585. [https://doi.org/10.1175/1520-0493\(2001\)129<0569:CAALSH>2.0.CO;2](https://doi.org/10.1175/1520-0493(2001)129<0569:CAALSH>2.0.CO;2).
- Chen W, Jiang Z, Li L. 2011. Probabilistic projections of climate change over China under the SRES A1B scenario using 28 AOGCMs. *J. Clim.* **24**: 4741–4756. <https://doi.org/10.1175/2011JCLI4102.1>.
- Christensen JH, Christensen OB. 2007. A summary of the PRUDENCE model projections of changes in European climate by the end of this century. *Clim. Change* **81**: 7–30. <https://doi.org/10.1007/s10584-006-9210-7>.
- Collins WD, Rasch P, Boville BA, Hack JJ, Mccaa J, Williamson DL, Kiehl JT. 2004. Description of the NCAR community atmosphere model (CAM 3.0). NCAR Technical Report No. TN-464+STR, NCAR, Boulder, CO.
- Jacob D. 2014. EURO-CORDEX: new high-resolution climate change projections for European impact research. *Reg. Environ. Change* **14**(2): 563–578. <https://doi.org/10.1007/s10113-013-0499-2>.
- Déqué M, Rowell D, Lüthi D, Giorgi F, Christensen J, Rockel B, Jacob D, Kjellström E, Castro MD, Hurk B. 2007. An intercomparison of regional climate simulations for Europe: assessing uncertainties in model projections. *Clim. Change* **81**(1): 53–70.
- Deser C, Phillips A, Bourdette V, Teng H. 2012. Uncertainty in climate change projections: the role of internal variability. *Clim. Dyn.* **38**(3–4): 527–546.
- Dufresne J, Foujols M, Denvil S, Caubel A, Marti O, Aumont O, Balkanski Y, Bekki S, Bellenger H, Benshila R, Bony S, Bopp L, Braconnot P, Brockmann P, Cadule P, Cheruy F, Codron F, Cozic A, Cugnet D, de Noblet N, Duvel J, Ethé C, Fairhead L, Fichefet T, Flavoni S, Friedlingstein P, Grandpeix J, Guez L, Guilyardi E, Haugustaine D, Hourdin F, Idelkadi A, Ghattas J, Joussaume S, Kageyama M, Krinner G, Labetouille S, Lahellec A, Lefebvre M, Lefevre F, Levy C, Li Z, Lloyd J, Lott F, Madec G, Mancip M, Marchand M, Masson S, Meurdesoif Y, Mignot J, Musat I, Parouty S, Polcher J, Rio C, Schulz M, Swingedouw D, Szopa S, Talandier C, Terray P, Viovy N, Vuichard N. 2013. Climate change projections using the IPSL-CM5 earth system model: from CMIP3 to CMIP5. *Clim. Dyn.* **40**(9–10): 2123–2165. <https://doi.org/10.1007/s00382-012-1636-1>.
- Easterling DR, Meehl GA, Parmesan C, Changnon SA, Karl TR, Mearns LO. 2000. Climate extremes: observations, modeling, and impacts. *Science* **289**(5487): 2068–2074.
- Editorial Committee of National Assessment Report of Climate Change. 2011. *Second National Assessment Report of Climate Change*. Science Press: Beijing, China.
- Emanuel KA, Zivkovic-Rothman M. 1999. Development and evaluation of a convection scheme for use in climate models. *J. Atmos. Sci.* **56**(11): 1766–1782.
- Fichefet T, Morales-Maqueza A. 1997. Sensitivity of a global sea ice model to the treatment of ice thermodynamics and dynamics. *J. Geophys. Res.* **102**(C6): 12609–12646. <https://doi.org/10.1029/97jc00480>.
- Gao X, Shi Y, Zhang D, Wu J, Giorgi F, Ji Z, Wang Y. 2012a. Uncertainties in monsoon precipitation projections over China: results from two high-resolution RCM simulations. *Clim. Res.* **52**: 213–226.
- Gao Y, Fu JS, Drake JB, Liu Y, Lamarque JF. 2012b. Projected changes of extreme weather events in the eastern United States based on a high resolution climate modeling system. *Environ. Res. Lett.* **7**(4): 044025. <https://doi.org/10.1088/1748-9326/7/4/044025>.
- Giorgi F, Mearns LO. 1999. Introduction to special section: regional climate modeling revisited. *J. Geophys. Res.* **104**: 6335–6352.
- Giorgi F, Christensen J, Hulme M, Storch HV, Whetton P, Jones R, Mearns L, Fu C, Arritt R, Bates B. 2001. *Regional Climate Information-Evaluation and Projections*. Cambridge University Press: Cambridge, UK.
- Giorgi F, Coppola E, Salomon F, Mariotti L, Sylla MB, Bi X, Elguindi N, Diro GT, Nair V, Giuliani G, Turuncoglu UU, Cozzini S, Guttler I, O'Brien TA, Tawiiq AB, Shalaby A, Zakey AS, Steiner AL, Stordal F, Sloan LC, Brankovic C. 2012. RegCM4: model description and preliminary tests over multiple CORDEX domains. *Clim. Res.* **52**(1): 7–29. <https://doi.org/10.3354/cr01018>.
- Grell GA, Dudhia J, Stauffer DR. 1994. A description of the fifth generation Penn State/NCAR mesoscale model (MM5). NCAR Report No. TN-398 STR, NCAR, Boulder, CO.
- Hazeleger W, Severijns C, Semmler T, Stefanescu S, Yang S, Wang X, Wyser K, Baldasano J, Bintanja R, Bougeault P, Caballero R, Dutra E, Ekman A, Christensen J, van den Hurk B, Jimenez P, Jones C, Källberg P, Koenigk T, MacGrath R, Miranda P, van Noije T, Schmitt T, Selten F, Storelvmo T, Sterl A, Tapamo H, Vancoppenolle M, Viterbo P, Wille U. 2010. EC-earth: a seamless earth system prediction approach in action. *Bull. Am. Meteorol. Soc.* **91**: 1357–1363. <https://doi.org/10.1175/2010BAMS 2877.1>.
- Holtslag MAA, Boville BA. 1993. Local versus nonlocal boundary-layer diffusion in a global climate model. *J. Clim.* **6**: 1825–1842.

- Hong SY, Dudhia J, Chen SH. 2004. A revised approach to ice microphysical processes for the bulk parameterization of clouds and precipitation. *Mon. Weather Rev.* **132**: 103–120. [https://doi.org/10.1175/1520-0493\(2004\)132<0103:ARATIM>2.0.CO;2](https://doi.org/10.1175/1520-0493(2004)132<0103:ARATIM>2.0.CO;2).
- Hong S-Y, Noh Y-H, Dudhia J. 2006. A new vertical diffusion package with an explicit treatment of entrainment processes. *Mon. Weather Rev.* **134**: 2318–2341.
- Hourdin F, Foujols M-A, Codron F, Guemas V, Dufresne J-L, Bony S, Denvil S, Guez L, Lott F, Ghattas J, Braconnot P, Marti O, Meurdesoif Y, Bopp L. 2013. Impact of the LMDZ atmospheric grid configuration on the climate and sensitivity of the IPSL-CM5A coupled model. *Clim. Dyn.* **40**(9–10): 2167–2192. <https://doi.org/10.1007/s00382-012-1411-3>.
- Hui P, Tang J, Wang S, Wu J, Kang Y. 2014. Future climate projection under IPCC A1B scenario in the source region of Yellow River with complex topography using RegCM3. *J. Geophys. Res. Atmos.* **119**(19): 11205–11222. <https://doi.org/10.1002/2014JD021992>.
- Hui P, Tang J, Wang S, Niu X, Zong P, Dong X. 2018. Climate change projections over China using regional climate models forced by two CMIP5 global models. Part I: evaluation of historical simulations. *Int. J. Climatol.* **38**: e57–e77. <https://doi.org/10.1002/joc.5351>.
- IPCC. 2013. *Climate Change 2013: The Physical Science Basis*. Cambridge University Press: Cambridge, UK and New York, NY.
- Jeong DI, Sushama L, Khalil MN. 2014. The role of temperature in drought projections over North America. *Clim. Change* **127**: 289–303.
- Kain JS. 2004. The Kain–Fritsch convective parameterization: an update. *J. Appl. Meteorol.* **43**(1): 170–181. [https://doi.org/10.1175/1520-0450\(2004\)043<0170:TKCPAU>2.0.CO;2](https://doi.org/10.1175/1520-0450(2004)043<0170:TKCPAU>2.0.CO;2).
- Kiehl JT, Hack JJ, Bonan GB, Boville BA, Williamson D, Rasch P. 1998. The National Center for Atmospheric Research Community climate model (CCM3). *J. Clim.* **11**: 1307–1326.
- Kim CS, Suh MS, Hong KO. 2009. Bayesian change point analysis of the annual maximum of daily and sub-daily precipitation over South Korea. *J. Clim.* **22**: 6741–6757.
- Krinner G, Viovy N, de Noblet-Ducoudré N, Ogée J, Polcher J, Friedlingstein P, Ciais P, Sitch S, Prentice IC. 2005. A dynamic global vegetation model for studies of the coupled atmosphere–biosphere system. *Global Biogeochem. Cycles* **19**(1): GB1015. <https://doi.org/10.1029/2003gb002199>.
- Lawrence DM, Fisher R. 2013. The community land model philosophy: model development and science applications. *iLEAPS Newslett.* **13**: 16–19.
- Lawrence DM, Oleson KW, Flanner MG, Thornton PE, Swenson SC, Lawrence PJ, Zeng X, Yang Z-L, Levis S, Sakaguchi K, Bonan GB, Slater AG. 2011. Parameterization improvements and functional and structural advances in version 4 of the community land model. *J. Adv. Model. Earth Syst.* **3**(1): 365–375. <https://doi.org/10.1029/2011MS000045>.
- Madec G. 2008. "NEMO Ocean Engine". Note du Pole de Mode'lisation. Institut Pierre-Simon Laplace (IPSL): Paris, France.
- Marengo JA, Ambrizzi T, Rocha RPD, Alves LM, Cuadra SV, Valverde MC, Torres RR, Santos DC, Ferraz SE. 2010. Future change of climate in South America in the late twenty-first century: intercomparison of scenarios from three regional climate models. *Clim. Dynam.* **35**(6): 1073–1097.
- Niu X, Wang S, Tang J, Lee D-K, Gao X, Wu J, Hong S, Gutowski WJ, McGregor J. 2015. Multimodel ensemble projection of precipitation in eastern China under A1B emission scenario. *J. Geophys. Res. Atmos.* **120**(19): 9965–9980. <https://doi.org/10.1002/2015jd023853>.
- Pal JS, Small EE, Eltahir EAB. 2000. Simulation of regional-scale water and energy budgets: representation of subgrid cloud and precipitation processes within RegCM. *J. Geophys. Res. Atmos.* **105**(D24): 29579–29594. <https://doi.org/10.1029/2000jd900415>.
- Qin P, Xie Z. 2016. Detecting changes in future precipitation extremes over eight river basins in China using RegCM4 downscaling. *J. Geophys. Res. Atmos.* **121**: 6802–6821. <https://doi.org/10.1002/2016JD024776>.
- Shiogama H, Emori S, Takahashi K, Nagashima T, Ogura T, Nozawa T, Takemura T. 2010. Emission scenario dependency of precipitation on global warming in the MIROC3.2 model. *J. Clim.* **23**(9): 2404–2417.
- Smiatek G, Kunstmann H, Senatore A. 2016. EURO-CORDEX regional climate model analysis for the greater alpine region: performance and expected future change. *J. Geophys. Res. Atmos.* **121**(13): 7710–7728. <https://doi.org/10.1002/2015jd024727>.
- Suh M-S, Lee D-K. 2004. Impacts of land use/cover changes on surface climate over East Asia for extreme climate cases using RegCM2. *J. Geophys. Res.* **109**: D02108. <https://doi.org/10.1029/2003JD003681>.
- Tang J, Niu X, Wang S, Gao H, Wang X, Wu J. 2016. Statistical downscaling and dynamical downscaling of regional climate in China: present climate evaluations and future climate projections. *J. Geophys. Res. Atmos.* **121**(5): 2110–2129. <https://doi.org/10.1002/2015jd023977>.
- Taylor K, Stouffer R, Meehl G. 2012. An overview of CMIP5 and the experiment design. *Bull. Am. Meteorol. Soc.* **93**: 485–498. <https://doi.org/10.1175/BAMS-D-11-00094.1>.
- Tiedtke M. 1993. Representation of clouds in large-scale models. *Mon. Weather Rev.* **121**: 3040–3061. <https://doi.org/10.1175/1520-0493.121.11.3040>.
- Valecke S. 2006. OASIS3 user guide (prism_2-5). Technical Report No. TR/CMGC/06/73, CERFACS, Toulouse, France.
- Wang W, Shao Q, Yang T, Yu Z, Xing W, Zhao C. 2014. Multimodel ensemble projections of future climate extreme changes in the Haihe River Basin, China. *Theor. Appl. Climatol.* **118**(3): 405–417. <https://doi.org/10.1007/s00704-013-1068-9>.
- Wu C, Huang G. 2016. Projection of climate extremes in the Zhujiang River basin using a regional climate model. *Int. J. Climatol.* **36**(3): 1184–1196. <https://doi.org/10.1002/joc.4412>.
- Yang H, Jiang Z, Li L. 2016. Biases and improvements in three dynamical downscaling climate simulations over China. *Clim. Dyn.* **47**: 3235–3251. <https://doi.org/10.1007/s00382-016-3023-9>.
- Zou L, Zhou T. 2013. Near future (2016–40) summer precipitation changes over China as projected by a regional climate model (RCM) under the RCP8.5 missions scenario: comparison between RCM downscaling and the driving GCM. *Adv. Atmos. Sci.* **30**(3): 806–818. <https://doi.org/10.1007/s00376013-2209-x>.
- Zou L, Zhou T. 2016. Future summer precipitation changes over CORDEX-East Asia domain under the RCP8.5 scenario downscaled by a regional ocean–atmosphere coupled model: a comparison to the stand-alone RCM. *J. Geophys. Res. Atmos.* **121**: 2691–2704. <https://doi.org/10.1002/2015JD024519>.